Scattering-Scanning Near-Field Optical Microscopy with Femtosecond Laser Pulses

by

Peter B. Van Blerkom

A thesis submitted to the

Faculty of the Graduate School of the

University of Colorado in partial fulfillment

of the requirements for the degree of

Masters of Science

Department of Physics

2016

This thesis entitled:
Scattering-Scanning Near-Field Optical Microscopy with Femtosecond Laser Pulses
written by Peter B. Van Blerkom
has been approved for the Department of Physics

_____

Prof. Markus Raschke

_____

Prof. Thomas Schibli

_____

Prof. Joseph Smyth

Date _____

The final copy of this thesis has been examined by the signatories, and we find that both the content and the form meet acceptable presentation standards of scholarly work in the above mentioned discipline.

Van Blerkom, Peter B. (M.S., Physics)

Scattering-Scanning Near-Field Optical Microscopy with Femtosecond Laser Pulses

Thesis directed by Prof. Markus Raschke

The macroscopic properties of materials we observe emerge from the collective structural configuration and dynamical behavior of the atomic or molecular constituents. Therefore, in order to fully characterize and understand these properties, it is necessary to develop measurement techniques capable of probing at these scales. Such a technique is that of combining scattering scanning near-field optical microscopy with ultrafast spectroscopy. Traditional, far-field microscopy is limited by diffraction, making it impossible to resolve details smaller than approximately half the wavelength of the illuminating light. However, the electromagnetic field that is produced when an object is illuminated is not simply characterized by the light that carries energy, radiating to the far-field, but also consists of a more structured rapidly decaying evanescent field. The structure of this evanescent, nonradiating near-field is not limited by diffraction, and so in measuring this field, it is possible to resolve the microstructure of matter in a way that is independent of the illuminating wavelength. By placing a metallic tip close enough to the surface to be within this evanescent field, the electric near-field is then scattered off of it, allowing it to be observed. Through the measurement of backscattered light off of nanometer scale probes developed for the use in scanning probe microscopy, near-field detection was realized in the form of scattering scanning near-field optical microscopy, allowing wavelength independent but spectroscopically sensitive imaging with nanoscale resolution. However, background interference from stray reflections usually overwhelm the back-scattered signal. By oscillating the tip at its mechanical resonant frequency, the near-field component of the signal can be detected in the anharmonic response to this modulation. This anharmonicity appears in the Fourier components of frequencies at integer multiples of the modulation frequency, a type of demodulation done through the use of a lock-in amplifier. However, a lock-in amplifier continuously samples the detector, while to obtain temporal resolution, a pulsed

laser sources are necessary. By measuring the response of a sample to an initial excitation with a time delayed secondary laser pulse in pump-probe spectroscopy, the time dependence of an excitation can be measured. However, if the repetition rate of this pulsed laser is close to the modulation frequency of the tip, a lock-in amplifier will have difficulty demodulating the near-field signal.

As an alternative to lock-in detection, we developed a method which synchronized data acquisition with the repetition rate of the laser pulse source, acquiring data only when the signal at the photodetector is at its maximum. In doing so, we were not only able to improve the signal quality as compared to that of a lock-in amplifier, as measured in the noise of approach curves over a gold surface and in a raster scan of a gold-silicon step edge, we were also able to apply an alternative method of near-field detection whereby we compared the curvature of the tip-scattered signal at the top and bottom of the tip-oscillation. This was similarly demonstrated in an approach curve over gold and in a raster scan over the step edge. Also, since the data were saved onto a computer, we were able to apply post-processing, enabling us to improve this method of curvature comparison, and create an approach curve showing a very clear near-field signal with little far-field interference. Therefore, in developing this data collection technique, we have demonstrated both an improvement to traditional lock-in detection when applied to pulsed laser sources along with a capability of implementing near-field reconstruction beyond that of harmonic demodulation.

Dedication

This thesis is dedicated to my parents, whose endless love and support has provided me with the strength I needed to persevere.

Acknowledgements

I would first like to first and foremost thank my advisor Prof. Markus Raschke, whose support has allowed me to make it this far.

I would also like to thank Eric Muller and Ronald Ulbricht for their significant contributions, advice, and assistance in this endeavor.

Contents

Chapter

Tables

Table

Figures

Figure

Chapter 1

Introduction

The matter in the world around us exhibits various observable properties, ranging from the seemingly mundane, such as an object's color, to the more exotic, such as superconductivity. All of these properties arise from the same, straightforward set of physical laws – those being the laws of quantum mechanics and electromagnetism. However, the macroscopic properties we observe cannot be found through direct application of these laws; instead they emerge from the sum of an ensemble of more fundamental microscopic structures. Therefore, we must develop probes capable of resolving this microstructure and observe the world at more natural length scales, thus providing the tools to determine the relationship between structure and function. Similarly, to understand the intrinsic electronic and vibrational properties of these sub-ensemble structures and how they interact, we must probe their dynamical response to energetic perturbation. Therefore, we also need a probe which is both faster than the lifetime of such excitations and with energetic tunability such that we can select which excitations to examine. The technique of ultrafast laser spectroscopy provides for us such a probe. In combining this technique with the technology of near-field optical microscopy, it becomes possible to observe this temporal evolution with nanoscopic spatial resolution, providing insight to the more fundamental behavior of matter.

1.1 Historical Survey

The first ventures into length scales smaller than our ability to perceive truly began in the seventeenth century with the development of the optical microscope, an object whose creation

ushered in an entire new era of science where the invisible microstructure of the world began to emerge. Initially, the field most affected was that of biology, where with the observation of cells in living matter by Robert Hooke in 1665 quickly brought the realization that all living creatures were composed of a more fundamental structure[16, 6].

Alongside this development naturally came more fundamental research into the behavior of light itself and its interactions with matter. In 1666, Sir Isaac Newton famously described the passage of sunlight through a prism, correctly concluding that white light was composed of a spectrum of colors, each one traveling at a different speed through the glass. More than a century later, in 1802 William Wollaston, upon implementing a more improved version of Newton's experiment, noticed that what initially appeared to be a continuous spectrum actually contained a regular pattern of dark lines, and so soon afterwards a device called the spectrometer was developed by optician Joseph von Fraunhofer to accurately measure the position of these strange absences of color. With the assistance of this device, it was noticed that the position, and therefore color of these various lines observed were dependent upon the chemical composition of the absorber or emitter. This observation laid the foundation of quantum mechanics; it was reasoned that because the colors emitted and absorbed by a system correspond to discrete values of energy, then the allowed states of the microscopic elements composing the system are themselves quantized, and so a new tool in the pursuit of probing the structure of the microscopic world was attained[30].

As the field of optical spectroscopy advanced, however, the microscope itself saw little improvement in resolution. In 1873 and 1879, E. Abbe and Lord Rayleigh respectively published their theories of resolution[1, 26], postulating an upper bound on the magnification power of an optical microscope, a diffraction limit with a value on the order of one half the wavelength of the light used ($\lambda/2$). This limitation forced the study of microscopic structure away from the optical regime and so other methods of structural determination were developed. X-ray diffraction (XRD) for instance takes advantage of the periodicity of crystalline solids and a wavelength of light on the order of the atomic separation of a lattice while scanning electron microscopy (SEM) capitalized upon the much shorter de-Broglie wavelength of an electron compared to that of a photon of comparable

energy, and so details much smaller than that observable by a visible microscope were obtained. However, the aforementioned techniques are limited to particular samples that can be studied and the information that can be obtained. An SEM, for example, requires a conductive surface while XRD requires long range periodicity and energies that can be destructive to soft matter.

The optical diffraction limit seemed to erect a barrier towards the goal of obtaining spectroscopic information with sub-diffraction limited spatial resolution. However, this diffraction limit was formulated by only taking the propagating electromagnetic (EM) fields into account. Through a simple application of Maxwell's Equations with a monochromatic plane wave incident upon a dielectric interface, refracted and/or reflected waves will be produced, carrying with them the energy of the incident wave. Under certain conditions, such as that of total internal reflection, a secondary field is created at the surface of the interface, but this evanescent field carries no energy, and so it was a reasonable assumption that only the propagating field, also called the far-field, could be measured. In 1928, E.H. Synge proposed a method to take advantage of the non-propagating evanescent near-field of an illuminated sample by shining light through a narrow aperture of sub-wavelength diameter held at a very small distance from the sample[28]. Although the state of technology at that time was not capable of producing such an instrument, the theory was further developed by J.A. O'Keefe in 1956[23], and shortly thereafter demonstrated acoustically by A.V. Baez in 1958[4]. The first electromagnetic demonstration was realized in 1972 by E.A. Ash and G. Nicholls using microwave 3 cm radiation to resolve structures below $\lambda/60$[2]. However, it took the technologies of scanning probe microscopy (SPM) to fully realize Synges proposal as the aperture-sample distance needed was too small to be accurately controlled without the feedback mechanisms developed for SPM. With the availability of this technology, the first demonstration of near-field scanning optical microscopy (NSOM)[1] was achieved in 1982 by D.W. Pohl, utilizing a metal coated sharpened quartz crystal with its apex exposed, demonstrating a resolving power of around $\lambda/20$[24]. The technology was further developed through the use of metal coated optical fibers as SPM probes,

[1] Both SNOM and NSOM have been used interchangeably, but NSOM has come to conventionally refer to aperture type near-field scanning microscopy while s-SNOM or a-SNOM is used for scattering (also called apertureless) scanning near-field optical microscopy

with an exposed apex acting as the aperture. However, this aperture based system carries limitations of its own: the transmissive properties of the fiber limits the usable wavelengths, and although a smaller tip can resolve smaller details, reducing the size of the aperture substantially reduces the field back-scattered through the fiber. To overcome this limitation, it was realized that a plain metallic tip could act to scatter the near-field, and so apertureless scattering SNOM (s-SNOM) was developed. This method was first demonstrated by M. Specht et al. in 1992, resulting in a resolving power of $\lambda/200$[27]. Since then, several improvements to the method of s-SNOM have been developed. In 1994, Y. Inouye and S. Kawata demonstrated the currently used method of lock-in signal detection as a major improvement to signal quality[18]. Later, interferometric and wavelength dependent methods of near-field detection in s-SNOM were developed by F. Zenhausern and A. Bek[35, 7].

1.2 Outline

In this thesis, I present a technique for resolving nanoscale spectroscopic details through a measurement scheme applied to a system incorporating a femtosecond pulsed laser source with a scattering type scanning near-field microscope, with the ultimate goal of developing a spectrally sensitive probe, capable of observing the ultrafast dynamics of a system at the nanoscale. This scheme consists of synchronizing the acquisition of the tip-scattered signal to the pulse rate of the laser, producing both an increase in the signal-to-noise ratio as compared to traditional continuous signal acquisition employed in most s-SNOM systems, as well as providing the means to analyze the collected data for reconstruction of the near-field response through methods alternative to those commonly used in the near-field optical microscopy. After establishing a theoretical background to near-field optical microscopy along with a description of the traditional methods employed, I will describe the system we developed and present the data collected using this system, demonstrating its capabilities. Subsequently, I will conclude with a discussion on the potential capabilities of this system and present ideas for further modification to improve its versatility.

Chapter 2

Background and Theory

2.1 The Optical Diffraction Limit

A simple way to obtain a limit in the resolving power of light can be done through an application of Fourier analysis. If we take a wave whose intensity envelope is a Gaussian function with standard deviation σ_x, the field envelope will be given as:

$$E(x) = E_0 e^{\frac{-x^2}{4\sigma_x^2}}. \tag{2.1}$$

Taking the Fourier transform of this into wavenumber (k) space, we have:

$$E(k) = \tilde{E}_0 e^{-\sigma_x^2 k^2}. \tag{2.2}$$

Taking the absolute square of this, we find that the standard deviation in k space is $\sigma_k = 1/(2\sigma_x)$. If we take the standard deviation as the uncertainty in position and momentum, Δx and Δk, and consider that any deviation from a Gaussian will only increase the standard deviation, we obtain the uncertainty relation:

$$\Delta k \Delta x \geq \frac{1}{2}. \tag{2.3}$$

And so to have an accurate measure of position (a small value of Δx), the spread in k will proportionally become larger. For a monochromatic plane wave, the wavenumber k is related to the wavelength λ by $k = 2\pi/\lambda$. Taking this as our spread in k, the uncertainty in x can be given by:

$$\Delta x \geq \frac{\lambda}{4\pi}. \tag{2.4}$$

This at first appears to be a hard limit to the resolving power of light. However, as we will see, the assumption that the maximum momentum spread in one dimension is limited by the total momentum does not always hold. While the total momentum, given by $|\vec{k}| = \sqrt{k_x^2 + k_y^2 + k_z^2}$ remains constant, if a situation exists where the wavevector in one dimension has an imaginary value, then the wavevectors in the other dimensions can become unlimited while still satisfying equation (2.4).

To derive a more formal resolution limit of a classical microscope such as the Rayeligh Criterion or the Abbe Limit, we first determine how a single pointlike emitter on the object plane will be mapped onto the image plane as it passes through a lens system.

The Abbe limit is found from an application of the paraxial approximation of an object being focused through a lens. The Abbe limit is given as:

$$\Delta x = \frac{\lambda}{2\mathrm{NA}}, \tag{2.5}$$

where NA is the numerical aperture of the lens equal to $n \sin\theta$, where n corresponds to the index of refraction[1].

A similar limit was later proposed by Lord Rayleigh. The most basic emitter is that of a point-dipole oriented along the object plane. This allows us to approximate the field at the lens as a plane-wave, and so the image formed can be found through the application of the Fraunhofer diffraction formula for a circular aperture. The Fraunhofer equation,

$$U(p,q) = \int\int G(\xi,\eta) e^{-\frac{2\pi i}{\lambda}(p\xi+q\eta)} d\xi d\eta, \tag{2.6}$$

describes the diffracted field $U(p,q)$ of a monochromatic plane-wave source transmitted through an aperture described by the function $G(\xi,\eta)$, where $G(\xi,\eta)$ is a constant at points in the opening, and zero at points outside the opening. If we take the aforementioned situation of a circular aperture and describe it with polar coordinates (ρ,θ) where we let,

$$\xi = \rho\cos\theta, \qquad \eta = \rho\sin\theta, \tag{2.7}$$

and similarly take the polar representation of a point P on the image formed from the source,

$$p = w\cos\psi, \qquad q = w\sin\psi, \tag{2.8}$$

and so for an aperture of radius a, the Fraunhofer equation becomes,

$$U(P) = C\int_0^a \int_0^{2\pi} e^{-ik\rho w\cos(\theta-\psi)}\rho d\rho d\theta. \tag{2.9}$$

The solution to equation (2.9) can be given by:

$$U(P) = C\pi a^2\left[\frac{2J_1(kaw)}{kaw}\right], \tag{2.10}$$

where J_1 is the Bessel function of first kind, and C is a constant determined by the intensity of the incoming wave, I_0. Therefore, the measured intensity on the screen is:

$$I(P) = |U(P)|^2 = I_0\left[\frac{2J_1(kaw)}{kaw}\right]^2, \tag{2.11}$$

also known as the Airy function[9]. Figure 2.1 shows how two points P and Q would appear on a screen at points P' and Q'.

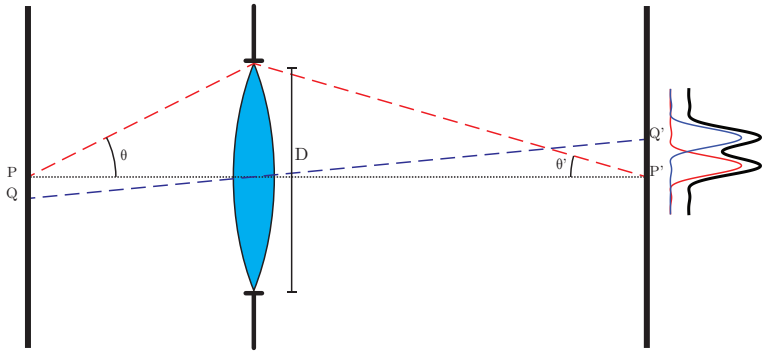

Figure 2.1: The imaging of two point emitters P and Q on the object plane as they project through a lens, forming two Airy disks at points P' and Q'

And so, Lord Rayleigh concluded that if two points on an object imaged by a lens were close enough so that the first zero of their point spread functions overlaps as in Figure 2.2, then the two points are unresolvable[26, 22].

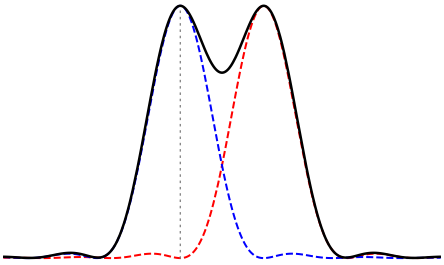

Figure 2.2: Two overlapping Airy functions separated such that they are centered over the first zero, demonstrating the Rayleigh diffraction limit

Solving (2.11) for the first zero, we find for a lens with numerical aperture $\mathrm{NA} = n \sin\theta$, the famous Rayleigh criterion:

$$\Delta y \approx 0.6098 \frac{\lambda}{\mathrm{NA}}. \tag{2.12}$$

2.2 Beyond the Diffraction Limit

2.2.1 The Near Field

The electromagnetic field can be decomposed into radiative and nonradiative components. The radiative portion carries energy (and information) to points far from the source and are therefore called the far-field. In contrast, the non-radiative fields tend to decay rapidly when measured further from the source, and are therefore called evanescent or near-field.

As described by H. Hertz in 1889, a radiating point dipole will have an electric field in Gaussian units given by[17, 19]:

$$\vec{E} = k^2 p(\hat{r} \times \hat{p}) \times \hat{r} \frac{e^{i(kr-\omega t)}}{r} + p\left[3(\hat{p} \cdot \hat{r})\hat{r} - \hat{p}\right]\left(\frac{1}{r^3} - \frac{ik}{r^2}\right) e^{i(kr-\omega t)}, \tag{2.13}$$

and magnetic field:

$$\vec{B} = k^2 p(\hat{r} \times \hat{p}) \left(\frac{1}{r} - \frac{1}{ikr^2}\right) e^{i(kr-\omega t)}, \tag{2.14}$$

for observation point $\vec{r} = r\hat{r}$, dipole moment $\vec{p} = p\hat{p}$, angular frequency ω, and wave number $k = \omega/c$. Inspecting (2.13), we can see that at large r, only the term proportional to $1/r$ will be

dominant. Furthermore, if we take the time averaged Poynting vector to determine the energy flow emitted by the dipole, we have:

$$\left\langle \vec{S} \right\rangle = \frac{c}{4\pi} \left\langle \vec{E} \times \vec{B} \right\rangle = \frac{ck^4 p^2 \sin\theta^2}{8\pi r^2} \hat{r}, \tag{2.15}$$

where θ is the angle between $\vec{r}$ and $\vec{p}$, we can see that only the terms proportional to $1/r$ contribute. This implies that the terms proportional to higher powers of $1/r$ do not contribute to the emission of energy and are therefore non-radiative, allowing for a distinction between the non-radiative near-field and the propagating far-field. This near-field configuration around a point dipole emitter is plotted in Figure 2.3, demonstrating the substantial deviation from the uniform field approximated by the plane-wave solution. Due to the extreme curvature of the field in the near-field regime, there is a larger spread in k when compared to that of plane-waves, which our solution approaches for large values of r. Therefore, if the near-field configuration could be measured, then a spatial resolution greater than the diffraction limit given by equation (2.5) can be achieved.

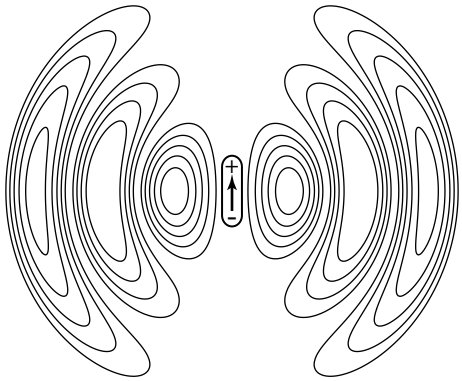

Figure 2.3: The electric field configuration close to a Hertzian dipole emitter

As mentioned earlier, if there exists a field configuration such that one of the components of $\vec{k}$ is imaginary, then the components in the other dimensions can become much larger than that of a simple plane-wave, allowing for sub-diffraction limited spatial resolution. Such a situation is realized in the rapidly decaying field present at the boundary between two mediums during processes such as total internal refraction.

2.2.2 Scattering Scanning Near-Field Optical Microscopy

To take advantage of the information contained in the near-field, we must find a method to propagate the near-field to the far-field as only then will it be measurable. s-SNOM achieves this through the scattering of the induced nonradiative electric field off of a conductive nanoscale probe.

Coupled Dipole Model

The scattering of an electric field off of a particle with radius $r \ll \lambda$ will be proportional to the polarizability of the particle [8], and so if we approximate the tip apex as a small particle with a polarizability modified by the sample being probed, we can determine the expected tip-scattered field as a function of the polarizability of the tip, the polarizability of the sample, and the distance between the two[3]. As a simplifying approximation, we can take the tip apex to be equivalent to a dielectric sphere with radius equal to the tip radius and relative permittivity $\epsilon = \epsilon_{\text{tip}}$. The polarizability of a sub-wavelength dielectric sphere is given by the Clausius-Mossotti relation[19],

$$\alpha = 4\pi r^3 \left(\frac{\epsilon_{\text{tip}} - 1}{\epsilon_{\text{tip}} + 2} \right). \tag{2.16}$$

With the tip a distance d from the surface of the sample, we can model the polarization response as that of an image dipole a distance d below the surface with relative strength of polarizability $\beta = (\epsilon_{\text{surf}} - 1)/(\epsilon_{\text{surf}} + 1)$ for surface permittivity ϵ_{surf}. This dual dipole system will then have a total effective polarizability along the vertical direction equal to[25]:

$$\alpha_{\text{eff}} = \alpha \left(1 - \frac{\alpha\beta}{16\pi d^3} \right)^{-1}. \tag{2.17}$$

This configuration is illustrated in Figure 2.4.

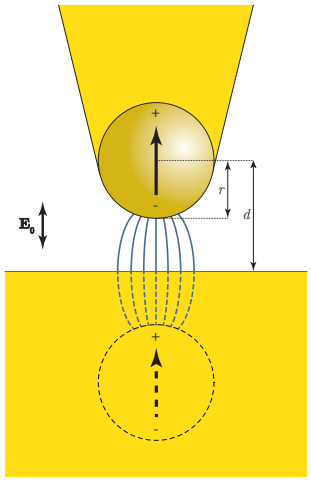

Figure 2.4: The approximation of a tip as a polarizable sphere with an image dipole below the substrate surface

Simulating the scattered field as being proportional to the absolute value of (2.17) with respect to tip-sample distance for a gold tip with a diameter of 20 nm over a gold sample, we create the approach curve seen in Figure 2.5

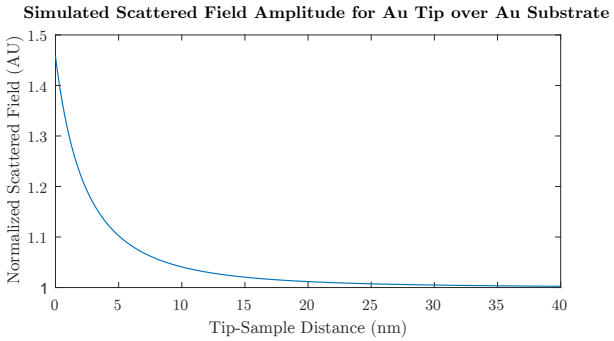

Figure 2.5: Simulation of the amplitude of scattered light with respect to tip-sample distance for a 20 nm diameter Au tip over an Au sample in the Coupled Dipole Model. The magnitude of the signal is normalized with respect to the signal as $d \to \infty$

Tapping-Mode AFM

As can be seen from Figure 2.5, the onset of the scattered near-field signal occurs within the ten or so nanometers. Although this has the benefit of spatially localizing the electric field to the same order as the tip radius, in order to actually produce a measurable signal, a mechanism capable of controlling the tip-sample distance with nanometer precision is necessary. This degree of control is achieved through the use of intermittent-contact-mode or tapping-mode atomic force microscopy (AFM). In tapping-mode AFM, the metal tip needed for scattering is attached to the end of a cantilever whose displacement from the sample surface is controlled by a piezoelectric actuator. A laser is reflected off of the end of the cantilever, and centered on a photodiode with four separate quadrants whose output voltage corresponds to the difference between the top and bottom or left and right quadrants, thereby acting as an accurate measure of the degree of cantilever deflection, as demonstrated in Figure 2.6. Through measuring this voltage, the AFM can maintain

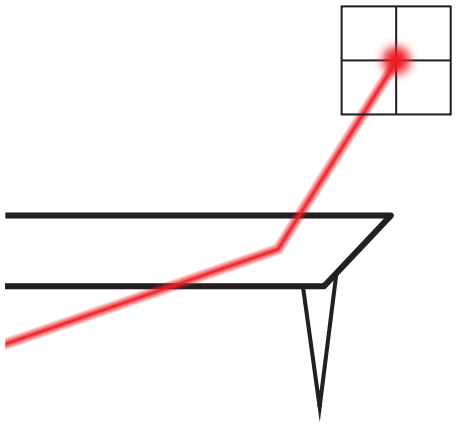

Figure 2.6: Reflection of the AFM control laser off the cantilever onto the quadrant photodiode

a constant force between the tip and the sample by adjusting the voltage to the height piezo until the quadrant photodiode voltage matches the user specified setpoint, and so in reading out the feedback voltage controlling the height piezo, the topography of the sample can be measured as the probe is scanned across the surface[13]. However, simply maintaining a constant distance from the

sample does not allow for meaningful measurements of the tip-scattered electric field, as a constant signal will be nearly indistinguishable from noise or background interference. In order to detect the tip-scattered signal, we apply a sinusoidal modulation to the cantilever at its resonant frequency, and so the desired signal will be similarly modulated. Taking the simulated tip-scattered signal of the coupled-dipole model from (2.17) and applying it to a sinusoidally oscillating cantilever with an amplitude of 20 nm, we produce the time-domain plot seen in Figure 2.7.

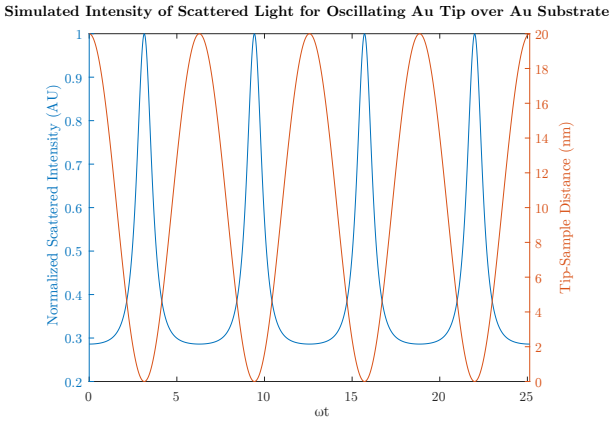

Figure 2.7: Simulation of the intensity of scattered light with respect to tip-sample distance for a 20 nm diameter Au tip over an Au sample in the Coupled Dipole Model for a tip oscillating with an amplitude of 20 nm

Background Interference and Harmonic Demodulation

The signal measured at the back-scattered light detection photodiode will not be solely from the tip-scattered light. Besides the normal background noise of ambient light, there are three sources of reflection which will overwhelm the tip-scattered signal. First, there is the light that back-reflects off of the irregularities of the mirrors and lenses along the beam-path. Second, there is the light reflected off of the sample as, due to diffraction, the laser cannot be focused to a spot-size comparable to the tip-radius, around 20 nm, but is instead focused to a spot size of around 10 µm, and so a region of the sample much larger than the tip radius will introduce back-scattered light

which is then focused onto the detector. Third, the tip shaft and cantilever will similarly backscatter. Considering only the first two terms, it would be a simple matter to find the tip-scattered signal as it will be dithered at the frequency of the tip. This signal could then be extracted using a device such as a lock-in amplifier, which measures the Fourier components of a signal at a specified frequency. With this, the modulated signal as seen in 2.7 can be selectively measured against the background signal. However, the background reflected off of the cantilever and shaft will be similarly modulated. To a first approximation, this modulated background signal will be linear with the cantilever motion, so if the background field is strong enough, the signal found by demodulating at the tip resonance will be overwhelmed by the background interference. As can be seen in 2.7, the tip-scattered signal is very nonlinear, and so the Fourier transform of the tip-scattered signal will have components not just at the cantilever modulation frequency, but at high harmonics–integer multiples of the fundamental frequency of the cantilever motion. This can be seen in Figure 2.8. Because of this, if we instead measure the lock-in demodulated signal at harmonics $n > 1$, we

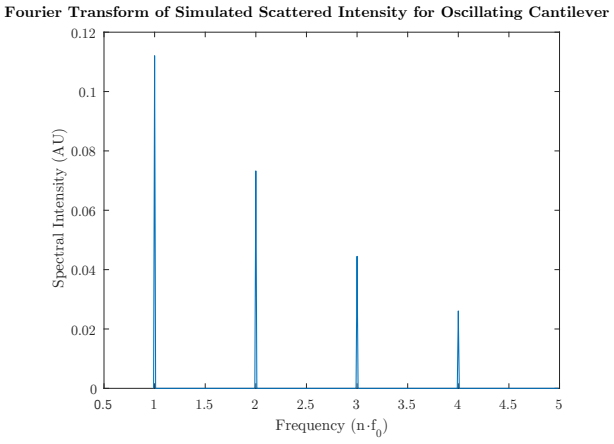

Figure 2.8: Normalized plot of the absolute Fourier transform of the signal shown in 2.7, demonstrating the existence of Fourier components at integer multiples of the modulation frequency f_0

should find a signal that directly corresponds to the strength of the near-field. This technique was demonstrated by Y. Inouye and S. Kawata in 1994[18].

Unfortunately, this is not the complete picture of background interference, since the field

from the shaft and cantilever will interfere with the other background sources, and so there will also be background interference beyond the first harmonic. P.G. Gucciardi, G. Bachelier, and M. Allegrini rigorously calculated the total background contribution to a detected signal, finding:

$$\mathrm{BKG}_{2n}(a_0, \Delta z) = 2 \cdot (-1)^n J_{2n}(2ka_0) \cdot [B_{FL}\cos(\phi_0) + B_{FS}\cos(\phi_2 + 2k\Delta z(t))], \tag{2.18}$$

for even harmonics $2n$ and:

$$\mathrm{BKG}_{2n+1}(a_0, \Delta z) = 2 \cdot (-1)^n J_{2n+1}(2ka_0) \cdot \left[B_{FL}\sin(\phi_0) + B^{FS}\sin(\phi_2 + 2k\Delta z(t))\right], \tag{2.19}$$

for odd harmonics $2n+1$, where a_0 is the tapping amplitude, $\Delta z(t)$ is the topographic sample height, $B_{FL} = 2|E_L E_F|$ and $B_{FS} = 2|E_S E_F|$ correspond to the background sources of the optics, E_L, the sample, E_S, and the tip shaft, E_F, the free-space wavenumber of the light k, and the phases ϕ_0 and ϕ_2 corresponding to phase differences introduced by the distances between the sample and the detector and the optics and the detector. J_n is the nth order Bessel function[15]. Despite the existence of background in all higher harmonics, the size of the background will decrease quickly at the higher harmonics. From this, it can be found that to first order in ka_0, that the ratio R_n of the background at the nth harmonic A_n to the DC background A_0 is:

$$R_n = \frac{|A_n|}{|A_0|} = \frac{2J_n(2ka_0)}{J_0(2ka_0)} \approx \frac{2}{n!}\left(\frac{2\pi a_0}{\lambda}\right)^n. \tag{2.20}$$

Two important consequences can be gleaned from equation (2.20). First, the background contribution to the signal decreases rapidly when demodulating at higher harmonics, and second, longer wavelengths λ also heavily decrease the background contribution.

Because of the strength of high-harmonic demodulation with a lock-in amplifier to reconstruct the near-field signal, with few exceptions[11], lock-in amplification is used ubiquitously in s-SNOM measurements.

2.3 Ultrafast Spectroscopy

The past two decades have seen the emergence of an arsenal of ultrafast laser sources along with techniques able to fully characterize the fields they produce, providing for us the means to probe the dynamics of a great variety of excitations and interactions once thought to occur too quickly to be observable[31, 34]. Such dynamics include those of chemical reactions, electronic and vibrational relaxations and couplings, and plasmon propagation[5, 36, 12]. The technique of pump-probe spectroscopy has been widely adopted as a powerful method of probing the dynamics of excitations. In pump-probe spectroscopy, an excitation is created through a pump pulse, whose spectrum is tuned to coincide with the excitation of interest. A probe pulse, usually of lower power, is sent after a controlled time delay to measure the state of the excited system in observing its absorption. By varying the time delay τ, the transient absorption can be observed, and so the dynamics of the excitation can be determined[14, 29]. Figure 2.9 shows a typical pump-probe setup.

A major attribute of s-SNOM that contributes to its versatility is in the ability to choose a laser source specific to the desired measurement, and so it is natural to combine the technique of ultrafast spectroscopy with that of near-field microscopy. In exciting a sample with a pump pulse and measuring the tip-scattered light of a time delayed probe pulse, the near-field response can be mapped in both space and time. Additionally, if the laser pulse is spectrally tunable, ultrafast s-SNOM then becomes capable of spatio-temporal spectroscopic nanoscale imaging, providing for us a tool capable of great insight into the properties and behavior of matter[3]. The work presented in this thesis is motivated by the goal to implement such a system.

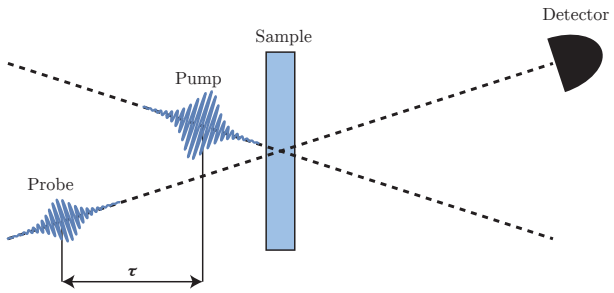

Figure 2.9: Typical pump-probe measurement, where the detector measures the change in absorption as the delay τ is varied

Chapter 3

Experimental Setup

The AFM we use is a Bruker Innova AFM modified for use in s-SNOM. Specifically, a beam-path was made to allow for the laser to be focused by an adjustable off-axis parabolic onto the tip. Our specific set-up is seen in Figure 3.1. Our laser source is a KM Labs Wyvern Ti-Sapphire laser producing 800 nm 50 fs pulses with an adjustable rep-rate with maximum usable value of around 300 kHz, capable of an average power output of 3 W.

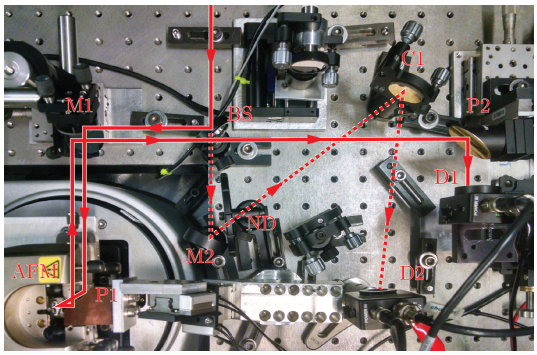

(a) Photograph of s-SNOM apparatus

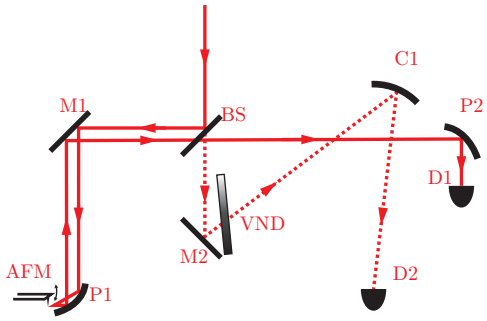

(b) Schematic of s-SNOM apparatus

Figure 3.1: s-SNOM apparatus, where BS is the beamsplitter, M1 is a periscope, P1 is the adjustable off-axis parabolic mirror, M2 is the reference beam mirror, VND is a variable neutral density filter, C1 is a spherical mirror for focusing the reference beam, P2 is the off-axis parabolic mirror for focusing the tip-scattered signal, D1 is the signal photodiode, D2 is the reference photodiode, and the Bruker Innova Atomic Force Microscope labeled AFM

3.1 Beyond the Lock-In Amplifier

Despite the aforementioned strengths of using a lock-in amplifier as a method of demodulating the tip-scattered near-field signal from the background interference, there exist several shortcomings when applied to certain situations. The situation which motivated our search for an alternative method of near-field detection is that of the incorporation of a pulsed laser source to an s-SNOM setup. Of principal benefit in using such a source is that it enables the technique of pump-probe spectroscopy, whereby an initial, relatively strong pump pulse excites the sample, and a delayed, usually weaker probe pulse is used to measure the state of the sample after it is allowed to evolve for an amount of time controlled by the separation of the two pulses, providing a method of measuring the sample response to the pump pulse in the time domain. Through tuning the pump and/or probe wavelength, we can gain information on the system with both spectral and temporal resolution. In applying a pump-probe scheme to a s-SNOM setup and measuring the backscattered probe pulse, we can produce information with temporal, spectral, and nanoscopic spatial resolution[34, 3].

Pump-probe spectroscopy is not the only benefit a femtosecond laser source can provide. As compared to a continuous wave (CW) laser source of the same average power, a femtosecond pulsed laser will produce much higher field intensities. For a 250 kHz 50 fs laser, the field magnitude will be on the order of 1×10^9 times greater than that of a CW laser. This is a desirable trait in s-SNOM as not only will the near-field response be enhanced, but nonlinear material responses such as second harmonic generation or frequency mixing can occur[10].

The issue faced in using a pulsed laser source with a lock-in amplifier is in its continuous sampling of the signal. Depending on the speed of the photodetector and the rep-rate of the laser, there will be periods of time between each pulse that the lock-in will be sampling either a greatly diminished signal, or nothing but the photodetector noise. This is especially problematic when the laser rep-rate is comparable to the driving tip resonance. A slower laser rep-rate can be desirable as the electric field magnitude can be much larger than that of a high rep rate laser for the same average power. Higher frequency tips are also desirable as their resonance will be much more stable

than that of a tip with a lower frequency resonance. Our setup falls under this situation, where we have AFM cantilevers with resonances around 250 kHz and a laser with a tunable rep rate between 200 kHz and 300 kHz.

Another drawback to a lock-in amplifier comes from the harmonic demodulation method of near-field reconstruction itself. Because the lock-in spreads the signal across all the harmonics, signal will be lost in each individual channel. Also, as seen in equations (2.18) and (2.19), the background contribution exists in all channels, which can be especially problematic for s-SNOM in the visible or near infrared. However, in using a lock-in, we are limited to only this harmonic demodulation scheme, and so we are unable to explore the possibility of other methods being better at reconstructing the near-field signal. For instance, as can be seen in Figure 2.5, the near-field response will only occur at the lower extrema of the tip oscillation, giving rise to a difference in curvature of the signal at opposite ends of the tip oscillation, as seen in Figure 2.7. Therefore, if we can find a way to measure the curvature of the signal from the photodetector and match it to the tip oscillation signal, comparing the absolute difference in curvature between the upper and lower extrema of the cantilever motion will be a measure of the tip-scattered near-field signal. Such a measurement can be seen to provide similar information to the lock-in detection method, as a difference in the curvature of the upper cycle to the lower cycle is a form of anharmonicity.

3.1.1 FPGA Data Collection

To implement an alternative method of data collection, we used a field programmable gated array (FPGA) as a device for enabling synchronized data acquisition. An FPGA is a device with a number of digital and analog input and output channels along with internal memory, capable of nearly arbitrary manipulation of the data read at its inputs, producing output signals determined by the program installed by the user.

Our program was designed to have as the analog input channels the raw photodiode signal, the AFM quadrant photodiode signal as a measure the cantilever position, along with a third channel which was used to either measure the reference photodiode signal for digital balancing

with the goal of subtracting the laser noise from the signal, or the z-piezo voltage as a measure of tip-sample height for the purpose of collecting approach curves. The digital input was the laser rep rate signal, a TTL (transistor-transistor logic) pulse which the laser control system would create whenever a laser pulse was launched.

To measure the signal, the FPGA would record the analog inputs only when the digital rep-rate laser transitioned from false (0 V) to true (5 V), synchronizing our data collection to the rep-rate of the laser, measuring the signal only when the pulse had scattered off the tip and has been subsequently detected by the photodetector. To do so, we also needed to introduce a delay to the pulse in order to synchronize the data collection with the least noisy portion of the photodiode signal. A raw trace of the voltage output of the photodiode and cantilever deflection is seen in Figure 3.2, where the desired measurement points occur near the peaks of the observed signal. A schematic of this setup can be seen in Figure 3.3 In measuring the cantilever position at the moment

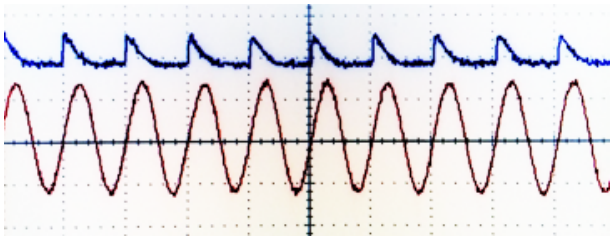

Figure 3.2: A oscilloscope trace of the raw cantilever motion (in red) and the photodiode signal (in blue). Their apparent synchronization is due to their frequencies being close in value

the pulse impacts the photodiode, we can correlate the two. This measured signal will appear as that of the signal a CW source would produce for a cantilever moving at the beat frequency between the true cantilever motion and the laser rep-rate. If we match the number of points collected to the per-pixel dwell time of the AFM, we can then apply whatever analysis scheme we desire and output that signal back to the AFM as an analog input instead of the usual lock-in signal, and take a scan as normal. For example, with a cantilever frequency of 250 kHz and a laser rep-rate of 260 kHz, we have a beat frequency of 10 kHz. A normal scan ran at 0.1 Hz with a horizontal sampling rate of 512 will have a dwell time of around 20 ms. In that time, the FPGA will gather around 5000

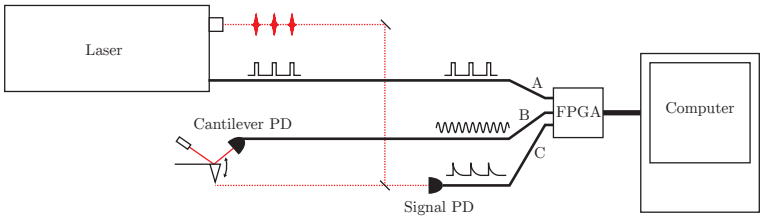

Figure 3.3: The laser produces a digital signal in channel A which corresponds to the laser pulses. The cantilever deflection is measured in analog channel B and the tip-scattered signal is measured in analog channel C. The FPGA then sends the measured signals to the computer through a PCI connection to be analyzed

points, which will have captured the signal throughout a total of around 50 tip oscillations.

Another prospective use of this method of data collection is that of post-processing. With the rep-rate of 260 kHz, 0.1 Hz scan speed, and a 512x512 image, a total of 1.3312×10^9 data points will be collected for each channel. If each data point was a 32 bit single floating-point number, this would produce a file of 5.325 GB in size. Although large, this is easily manageable by modern computer architecture. With these data offloaded to a computer, we can not only process the data with techniques that are more computationally expensive and so cannot be done in real-time, but we are not limited by the number of analog channels the FPGA can output or that the AFM can record.

Differential Curvature

It is a simple process of taking the Fourier transform of each block of data for each pixel and outputting its magnitude at the desired harmonic to reproduce the signal that would be acquired by a lock-in amplifier, with the additional benefit of synchronizing the sample rate with the laser rep-rate. However, as was mentioned earlier, other methods of real-time near-field reconstruction can be performed. The method we implemented was to calculate an approximation of the curvature of the tip-scattered signal at the turning points of the cantilever. This method should be at least equivalent to that of high-harmonic demodulation, as in measuring magnitude of the higher harmonics, we are effectively measuring the deviation of the signal from a normal sinusoid, a deviation which will

also appear as a difference in the curvature between the two extrema of oscillation. Furthermore, any portion of the interference from the far-field that is symmetric with respect to the upper and lower cycle of the tip oscillation will similarly have a symmetric contribution to the curvature at those two points, and so a measure of the difference in curvature will be effectively insensitive to any far-field contribution with such a form.

To calculate this approximation of the curvature, we take as an input two threshold values T_1 and T_2, the signal at index i, S_i, and the cantilever value at index i, C_i. Then, to calculate which signal points S_i fall between the extrema of the cantilever signal, maximum M and minimum m, we create the Boolean arrays:

$$B^U_{T_1,i} = \begin{cases} 1 & \text{if} \quad C_i \geq M(1-T_1) \\ 0 & \text{if} \quad C_i < M(1-T_1) \end{cases}, \tag{3.1}$$

and

$$B^L_{T_1,i} = \begin{cases} 1 & \text{if} \quad C_i \leq m(1-T_1) \\ 0 & \text{if} \quad C_i > m(1-T_1) \end{cases}. \tag{3.2}$$

With these arrays, we then find the mean of all the signal points S_i falling between the maximum and this threshold,

$$U_1 = \frac{\sum_i (S_i B^U_{T_1,i})}{\sum_i B^U_{T_1,i}}, \tag{3.3}$$

and

$$L_1 = \frac{\sum_i (S_i B^L_{T_1,i})}{\sum_i B^U_{T_1,i}}. \tag{3.4}$$

This process is repeated again for the signal for points falling between T_1 and T_2 of the cantilever signal,

$$B^U_{T_2,i} = \begin{cases} 1 & \text{if} \quad M(1-T_2) \leq C_i < M(1-T_1) \\ 0 & \text{if} \quad C_i < M(1-T_2)) \end{cases}, \tag{3.5}$$

and

$$B^L_{T_2,i} = \begin{cases} 1 & \text{if} \quad m(1-T_2) \geq C_i > m(1-T_1) \\ 0 & \text{if} \quad C_i > m(1-T_2)) \end{cases} \tag{3.6}$$

Similarly finding the mean of the signal at those points:

$$U_2 = \frac{\sum_i (S_i B^U_{T_2,i})}{\sum_i B^U_{T_2,i}}, \tag{3.7}$$

and

$$L_2 = \frac{\sum_i (S_i B^L_{T_2,i})}{\sum_i B^L_{T_2,i}}. \tag{3.8}$$

To find an approximation of the curvature, we then take the absolute difference between the two values,

$$\delta_U = |U_1 - U_2|, \tag{3.9}$$

and

$$\delta_L = |L_1 - L_2|. \tag{3.10}$$

The normalized approximate differential curvature (ADC) is then:

$$\Delta = \frac{|\delta_U - \delta_L|}{\delta_U + \delta_L}. \tag{3.11}$$

This scheme is demonstrated in Figure 3.4. An actual signal trace recorded by the FPGA is shown in 3.5 with the L_1 and L_2 points for a single cycle indicated in red and blue respectively.

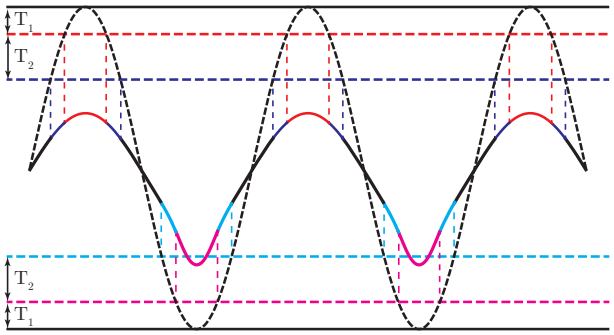

Figure 3.4: A demonstration of the determination of approximate differential curvature, where the solid, anharmonic oscillation represents the tip-scattered signal and the dashed oscillation represents the cantilever signal. The mean of the red points correspond to U_1, the blue points to U_2, the magenta points to L_1 and the cyan points as L_2. The red and magenta lines indicate T_1, and the blue and cyan lines indicate T_2

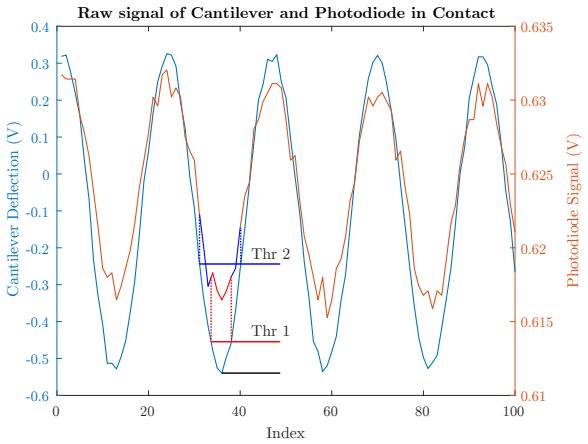

Figure 3.5: The FPGA measured photodiode and cantilever signal with points within the two thresholds indicated for the lower half of a single cycle

Chapter 4

Results

4.1 Preliminary Tests

To first test our method of data collection, we created a synthetic signal produced by an arbitrary waveform generator. We used a 100 kHz sine wave for the cantilever signal, a 110 kHz square wave as the digital rep-rate signal, and 100 kHz 50 mV and 5 mV sawtooth waves as the synthetic tip-scattered signal. A sawtooth wave was used as its Fourier components are well characterized, where the magnitude of its nth Fourier component is equal to $2A/(\pi n)$ for peak-to-peak amplitude A. The program, made in Lab-View, produces a readout that can be seen in Figure 4.1 for the 50 mV wave. The fundamental frequency of the simulated cantilever signal is seen as the maximum in the lower right panel, where higher harmonics are clearly visible. The values we

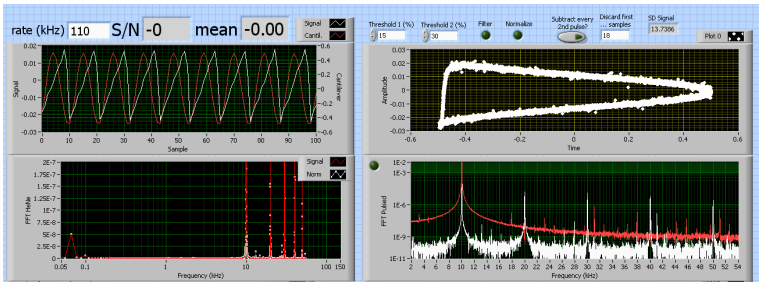

Figure 4.1: Lab-View front-panel output of the 50 mV test function. Upper left panel shows raw signal with simulated cantilever in red and sawtooth signal in white. The upper right panel shows the period trace of the signal with respect to the cantilever. The lower right panel shows a magnified FFT of the cantilever signal. The Lower right panel shows the FFT of the sawtooth signal in white and the cantilever signal in red

measured for this synthesized signal are seen in Table 4.1, where the ratios are calculated as the ratio of subsequent harmonics, producing a theoretical value of $n/(n+1)$ for the nth harmonic. Although the ratios do not correspond to the theoretical values, it is possible that this is a result

Table 4.1: 50 mV and 5 mV synthesized signal as measured by the FPGA and Lock-In Amplifier measured as the ratio of subsequent harmonics defining first harmonic to be equal to 1

Harmonic	50 mV Lock-In	50 mV FPGA	5 mV Lock-In	5 mV FPGA	Theory
1	1	1	1	1	1
2	0.51	0.16	0.5	0.16	0.5
3	0.66	0.8	0.65	0.8	0.66
4	0.75	0.54	0.75	0.5	0.75
5	Below noise	0.31	Below noise	0.33	0.8

of the total signal being spread over multiple frequency index values. However, it is promising that the FPGA recorded the same values for both the 50 mV and 5 mV signals. Also, the signal trace as seen in the upper left plot of Figure 4.1 does appear to be the correct waveform, albeit with some distortion. This, however, is a situation where the lock-in would be more capable, as the synthesized signal was more equivalent to a CW source than a pulsed source. Despite this apparent issue, when the FPGA was tested with a sinusoid, the expected result of no harmonics higher than $n = 1$ was indeed observed, so at this point it was unclear if the FPGA would produce a signal equivalent to the lock-in amplifier, so testing with a real tip-scattered signal from a pulsed laser source was necessary to measure its capabilities.

4.2 Comparisons with Lock-In Amplifier

To compare the FPGA synchronized data collection scheme with the lock-in amplifier, we took approach curves over a gold-silicon step edge sample, with the both FPGA and lock-in outputting second harmonic. The cantilever had a resonance of around 248 kHz and the rep-rate was set to 260 kHz. As can be seen in Figure 4.2, we can confirm not only that the FPGA program produces a signal equivalent to that of the lock-in amplifier, but it appears to have a better signal-to-noise

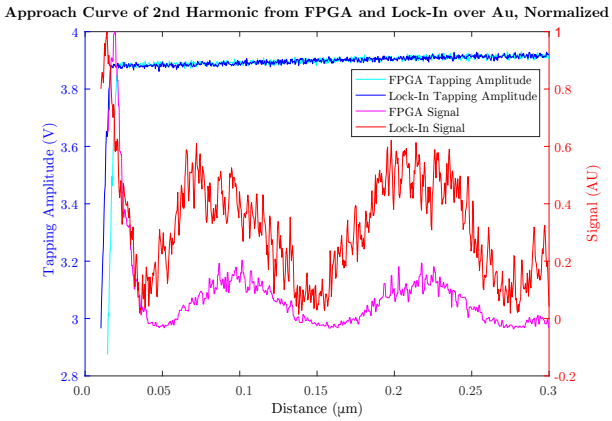

Figure 4.2: Approach over Au with FPGA and Lock-In outputting Second Harmonic

ratio than the lock-in. Also, it can be surmised that the signal measured is indeed near-field due to the sharp increase in signal which occurs before the tip makes contact (being the cusp of the tapping amplitude). To ensure that near-field was being measured, we repeated this over silicon, and as can be seen in Figure 4.3, both measured equivalent far-field interference fringes, but no near-field signal can be seen. We then took a 5 µm scan over the Si-Au step edge, as shown in Figure 4.4. This scan was done collecting both the lock-in second harmonic signal and the FPGA second harmonic signal simultaneously. The FPGA signal is sharper than the lock-in signal, indicating a better performance than the lock-in amplifier.

4.3 Absolute Differential Curvature

In the pursuit of an alternative to harmonic demodulation, we implemented the method discussed in section 3.1.1 to the same Si-Au step edge scanned in Figure 4.4. Initially, we took approach curves of the ADC, first with threshold values of $T_1 = 15\,\%$ and $T_2 = 30\,\%$ which can be seen in Figure 4.5, then with threshold values of $T_1 = 30\,\%$ and $T_2 = 60\,\%$, shown in Figure 4.6. The results of these scans, along with a lock-in amplifier output of second harmonic can be seen in Figure 4.7. Both of these approach curves appear to demonstrate significant near-field signal with minimal far-field interference indicating that this simple method of approximating the

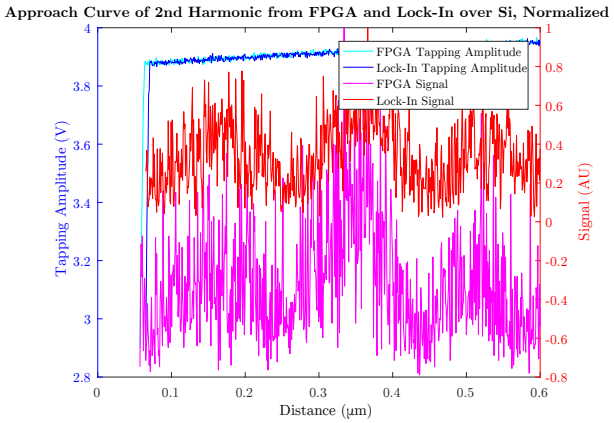

Figure 4.3: Approach over Si with FPGA and lock-In outputting second harmonic

differential curvature can indeed sere to characterize near-field. These curves also demonstrate the trade-off between signal-to-noise ratio and far-field interference when choosing a desired threshold value. Next, we took a scan near the same 5 µm area from Figure 4.4, measuring the ADC at the same two pairs of threshold values from the approach curves in Figures 4.5 and 4.6. The result of these scans are shown in Figure 4.7 alongside a lock-in second harmonic scan for comparison.

These scans clearly indicate that not only does the approximate differential curvature indeed indicate the presence of near-field, but that it may do so better than a lock-in amplifier demodulation.

4.4 Post-Processing

Although we can use the FPGA to output a calculated signal in real-time, allowing us to take advantage of the existing analog inputs of the AFM, if we instead save the dataset to the computer, we can perform any sort of post-processing analysis we desire.

4.4.1 Post-Processed Harmonic Demodulation

We collected a dataset to the computer throughout the duration of an approach while recording the cantilever, photodiode, and z-piezo voltages as our inputs. In collecting the z-piezo voltage,

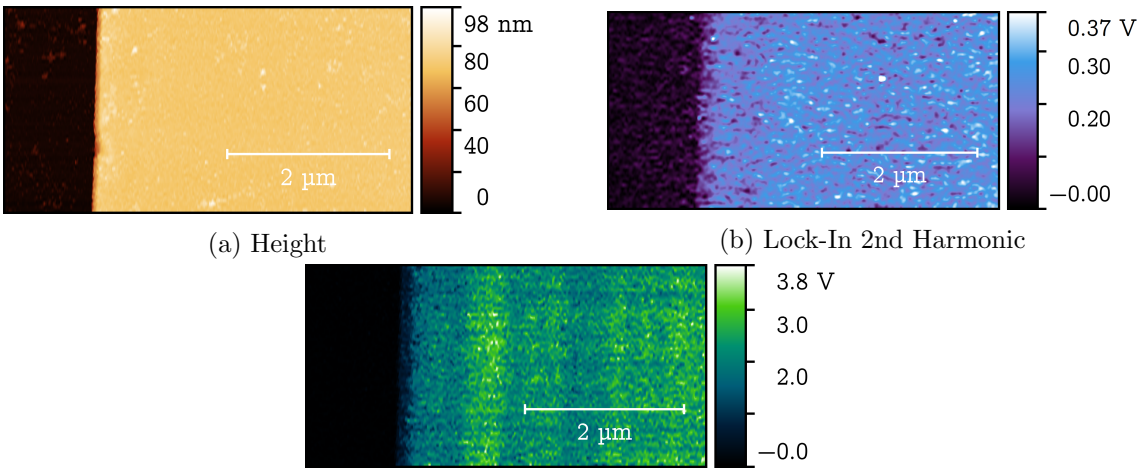

(a) Height

(b) Lock-In 2nd Harmonic

(c) FPGA 2nd Harmonic

Figure 4.4: 5 µm s-SNOM scan over Si-Au step edge with FPGA and Lock-In outputting 2nd harmonic

we are able to take any calculated value and correlate it with the tip-sample hight the, producing an approach curve for any calculated value we create. First, we took the FFT of the photodiode signal. We were able to observe a signal at third harmonic as can be seen in Figure 4.8. This was surprising as we were unable to observe third harmonic in the lock-in amplifier.

4.4.2 Post-Processed Differential Curvature

With the same dataset, we then used a similar technique to that of calculating the approximate differential curvature, but instead we of simply taking the difference between two values, we directly calculated the numerical third derivative of the photodiode signal, and took the average of that value within a single threshold for the upper and lower turning points. We repeated this process for several different threshold values and calculated the signal-to-noise ratio by taking the ratio of the maximum signal to the mean in an attempt to determine the threshold value which produced the best signal. The result of this can be seen in Figure 4.9, where a clear peak is seen at a threshold of 15 %. The approach curve of the differential curvature at this threshold can be seen in Figure 4.10. This approach curve demonstrates a significant lack of far-field interference, providing a substantial indication that not only does a calculation of the differential curvature

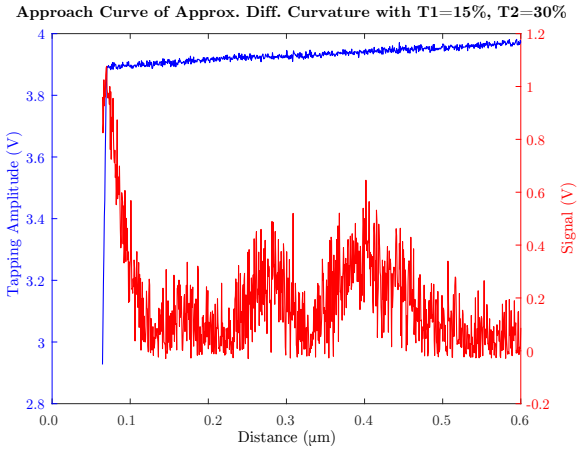

Figure 4.5: Approximate Differential Curvature approach over Au with $T_1 = 15\,\%$ and $T_2 = 30\,\%$

produce quality near-field signal, but that it may actually surpass harmonic demodulation in its ability to decrease far-field interference.

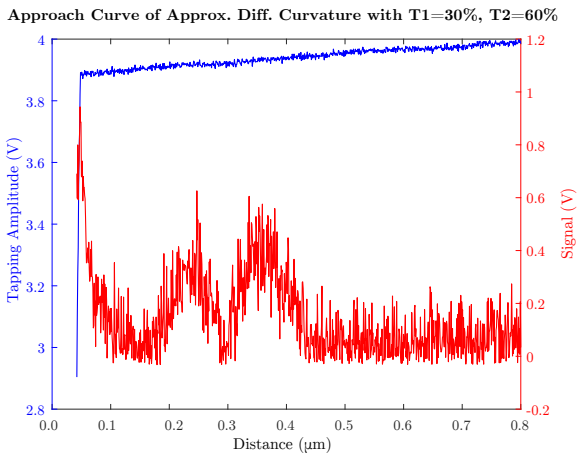

Figure 4.6: Approximate Differential Curvature approach over Au with $T_1 = 30\,\%$ and $T_2 = 60\,\%$

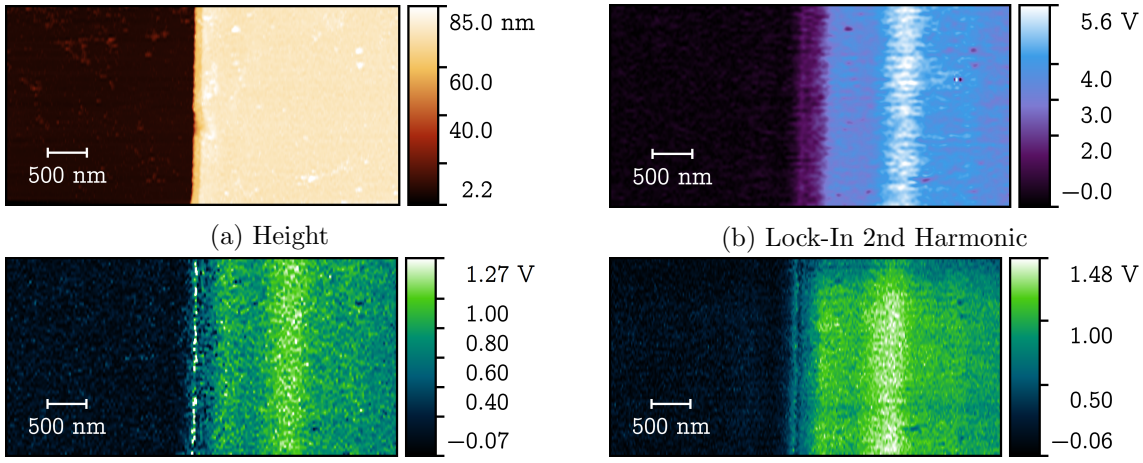

(a) Height

(b) Lock-In 2nd Harmonic

(c) ADC with $T_1 = 15\,\%$ and $T_2 = 30\,\%$

(d) ADC with $T_1 = 30\,\%$ and $T_2 = 60\,\%$

Figure 4.7: 5 µm s-SNOM scan over Si-Au step edge measuring approximate differential curvature for different threshold values

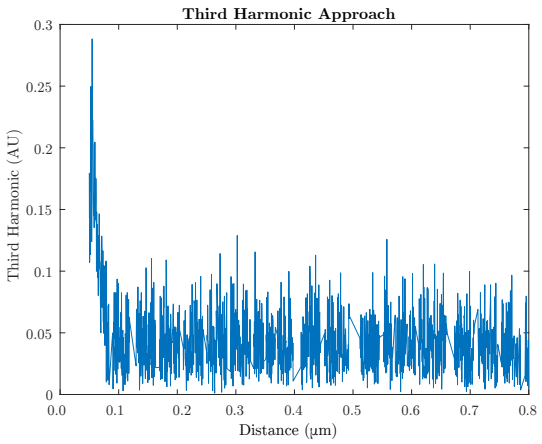

Figure 4.8: Approach Curve of third harmonic signal from post-processed data

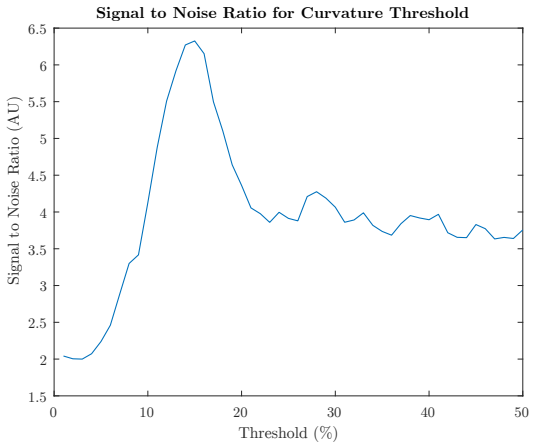

Figure 4.9: Signal-to-noise ratio versus threshold value for post-processed differential curvature approach

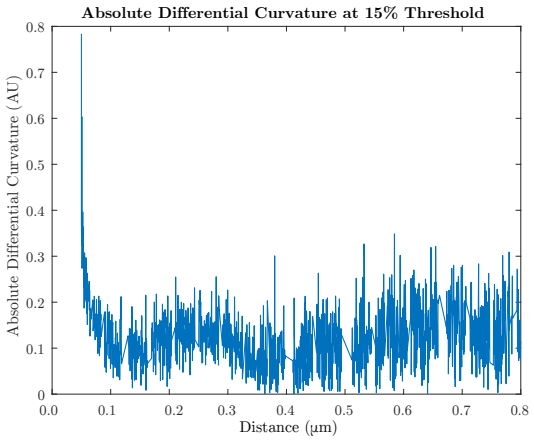

Figure 4.10: Approach Curve of post-processed differential curvature with a threshold of 15 %

Chapter 5

Discussion

Ultrafast pump-probe near-field optical imaging has been accomplished in NSOM systems[21, 20, 32] and with high repetition rate lasers in s-SNOM[33], and now with the method we have developed, we can apply ultrafast techniques to s-SNOM with low rep rate lasers without the usual accompanied loss of signal quality. Furthermore, we have demonstrated an alternative method of near-field measurement besides that of high-harmonic demodulation, and have provided qualitative evidence in its ability to measure near-field. However, a mathematically rigorous proof of such a method's capability of measuring near-field is yet to be shown. Although high-harmonic demodulation is a method of near-field reconstruction which is well established to be effective, due to the existence of far-field interference in the higher harmonics, especially for s-SNOM in visible wavelengths, investigating the possibility of alternative methods of near-field reconstruction remains a worthwhile endeavor, one which has been made possible by the synchronized data collection scheme developed in this work.

5.1 Future Prospects

This paper details only the preliminary work towards the ultimate goal of full near-field pump-probe spectroscopy, and so further work is necessary in pursuit of that goal. Meanwhile, other methods of near-field reconstruction could be explored, such as deconvolving the measured signal with that of a theoretical functional form of the far-field interference term.

The FPGA used throughout this paper was one with a $\pm 10\,\mathrm{V}$ analog input range with a bit

depth of 16. Since the signals in question rarely go beyond 2 V in magnitude, a data acquisition (DAQ) device with a smaller or variable voltage range could improve the SNR. We are currently in the process of installing such a DAQ as an upgrade to the FPGA we are using. Similarly, the FPGA only has 3 direct data channels, so if we want to capture x, y, z, cantilever deflection, tip-scattered signal, and a reference signal to completely bypass the AFM software, we will require additional data pathways, which the DAQ can provide.

Chapter 6

Conclusions

In the pursuit of a deeper and more fundamental understanding of the world around us, we design probes to push at the boundaries of spatial and temporal resolution. s-SNOM is such a tool, providing for us the means to bypass limits once thought to be insurmountable, especially in the unification of this technology with that of the femtosecond laser pulse. However, in the undertaking of this unification, the traditional implementations of data collection in near-field microscopy need to be reconsidered. Specifically, the method of near-field detection ubiquitous to s-SNOM, lock-in demodulation, was found to be wanting when applied to femtosecond laser sources with pulse repetition rates comparable to the tip dither frequency. We therefore introduced an alternative method of near-field detection, where data collection is synchronized to the laser rep-rate through the use of an FPGA. We demonstrated that this signal acquisition technique does indeed produce data with decreased noise levels as compared to the lock-in amplifier. We were also able to demonstrate the adaptability of synchronized data acquisition in the implementation of near-field reconstruction method alternative to harmonic demodulation–that of comparing the upper and lower curvature of the tip-scattered signal at the turning points of the cantilever oscillation. We were able to show that such a method was capable of producing compelling approach curves and scans, with near-field signal easily comparable to that of harmonic demodulation. In doing so, we demonstrated a method of near-field detection completely novel to the field of s-SNOM. Finally, as the FPGA allows us to save data to a computer hard-disk, we are able to apply various post-processing techniques. Through these achievements, this work has enabled a more robust method

of data collection in the pursuit of developing a system to acquire simultaneous temporal, spectral, and spatial resolution.

Bibliography

[1] E. Abbe, Beiträge zur theorie des mikroskops und der mikroskopischen wahrnehmung, Archiv für mikroskopische Anatomie, 9 (1873), pp. 413–418.

[2] E. A. Ash and G. Nicholls, Super-resolution aperture scanning microscope, Nature, 237 (1972), pp. 510–512.

[3] J. M. Atkin, S. Berweger, A. C. Jones, and M. B. Raschke, Nano-optical imaging and spectroscopy of order, phases, and domains in complex solids, Advances in Physics, 61 (2012), pp. 745–842.

[4] A. V. Baez, Is resolving power independent of wavelength possible? an experiment with a sonic "macroscope", Journal of the Optical Society of America, 46 (1956), p. 901.

[5] M. Bai, C. Guerrero, S. Ioanid, E. Paz, M. Sanz, and N. García, Measuring the speed of a surface plasmon, Physical Review B, 69 (2004), pp. 115416–1–115416–6.

[6] D. Bardell, The invention of the microscope, BIOS, 75 (2004), pp. 78–84.

[7] A. Bek, R. Vogelgesang, and K. Kern, Apertureless snom with sub-10 nm resolution, Review of Scientific Instruments, 77 (2006), pp. 043703–1–043703–11.

[8] C. Bohren, Absorption and scattering of light by small particles, Wiley, New York, New York, 1983.

[9] M. Born and E. Wolfe, Principles of Optics, Cambridge University Press, Cambridge, New York, 7 ed., 1999.

[10] R. Boyd, Nonlinear Optics, Academic Press, Burlington, Massachusetts, 3 ed., 2008.

[11] M. Brehm, A. Schliesser, and F. Keilmann, Spectroscopic near-field microscopy using frequency combs in the mid-infrared, Optics Express, 14 (2006), pp. 11222–11233.

[12] J. Diels and W. Rudolph, Ultrashort Laser Pulse Phenomena, Academic Press, Cambridge, Massachusetts, 2 ed., 2006.

[13] P. Eaton and P. West, Atomic Force Microscopy, Oxford University Press, Oxford, New York, 2010.

[14] E. M. Grumstrup, M. M. Gabriel, E. E. M. Cating, E. M. V. Goethem, and J. M. Papanikolas, Pump-probe microscopy: Visualization and spectroscopy of ultrafast dynamics at the nanoscale, Chemical Physics, 458 (2015), pp. 30–40.

[15] P. G. Gucciardi, G. Bachelier, and M. Allegrini, Far-field background suppression in tip-modulated apertureless near-field optical microscopy, Journal of Applied Physics, 99 (2006), pp. 124309–1–124309–9.

[16] E. Hecht, Optics, Addison-Wesley, Reading, Massachusetts, 4 ed., 2002.

[17] H. Hertz, The forces of electric oscillations treated according to maxwell's theory, Nature, 39 (1889), pp. 450–452.

[18] Y. Inouye and S. Kawata, Near-field scanning optical microscope with a metallic probe tip, Optics Letters, 19 (1994), pp. 159–161.

[19] J. D. Jackson, Classical Electrodynamics, Wiley, New York, New York, 3 ed., 1998.

[20] K. Karki, M. Namboodiri, T. Z. Khan, and A. Materny, Pump-probe scanning near field optical microscopy: Sub-wavelength resolution chemical imaging and ultrafast local dynamics, Applied Physics Letters, 100 (2012), p. 153103.

[21] B. A. Nechay, U. Siegner, M. Achermann, H. Bielefeldt, and U. Keller, Femtosecond pump-probe near-field optical microscopy, Review of Scientific Instruments, 70 (1999), p. 2758.

[22] L. Novotny and B. Hecht, Prinicples of Nano-Optics, Cambridge University Press, Cambridge, New York, 2006.

[23] J. A. O'Keefe, Resolving power of visible light, Journal of the Optical Society of America, 46 (1956), p. 359.

[24] D. W. Pohl, W. Denk, and M. Lanz, Optical stethoscopy: Image recording with resolution $\lambda/20$, Applied Physics Letters, 44 (1984), p. 651.

[25] M. B. Raschke and C. Lienau, Apertureless near-field optical microscopy: Tip-sample coupling in elastic light scattering, Applied Physics Letters, 83 (2003), pp. 5089–5091.

[26] Rayleigh, XXXI. investigations in optics, with special reference to the spectroscope, Philisophical Magazine Series 5, 8 (1879), pp. 261–274.

[27] M. Specht, J. D. Pedarnig, W. M. Heckl, and T. W. Hänsch, Scanning plasmon near-field microscope, Physical Review Letters, 68 (1992), pp. 476–479.

[28] E. H. Synge, XXXVIII. a suggested method for extending microscopic resolution into the ultra-microscopic region, The London, Edinburgh, and Dublin Philosophical Magazine and Journal of Science, 6 (1928), pp. 356–362.

[29] N. Tamai, T. Asahi, and H. Masuhara, Femtosecond transient absorption microspectrophotometer combined with optical trapping technique, Review of Scientific Instruments, 64 (1993), pp. 2496–2503.

[30] N. C. Thomas, The early history of spectroscopy, Journal of Chemical Education, 68 (1991), pp. 631–634.

[31] R. Trebino, Frequency-Resolved Optical Gating: the Measurement of Ultrashort Laser Pulses, Springer, New York, New York, 2000.

[32] A. Vertikov, M. Kuball, A. V. Nurmikko, and H. J. Maris, Time-resolved pump-probe experiments with subwavelength lateral resolution, Applied Physics Letters, 69 (1996), p. 2465.

[33] M. Wagner, Z. Fei, A. S. McLeod, A. S. Rodin, W. Bao, E. G. Iwinski, Z. Zhao, M. Goldflam, M. Liu, G. Dominguez, M. Thiemens, M. M. Fogler, A. H. C. Neto, C. N. Lau, S. Amarie, F. Keilmann, and D. N. Basov, Ultrafast and nanoscale plasmonic phenomena in exfoliated graphene revealed by infrared pump-probe nanoscopy, Nano Letters, 14 (2014), pp. 894–900.

[34] A. Weiner, Ultrafast Optics, Wiley, Hoboken, New Jersey, 2009.

[35] F. Zenhausern, Y. Martin, and H. K. Wickramasinghe, Scanning interferometric apertureless microscopy: Optical imaging at 10 angstrom resolution, Science, 269 (1995), pp. 1083–1085.

[36] A. H. Zewail, Femtochemistry: Atomic-scale dynamics of the chemical bond, Journal of Phiscial Chemistry A, 104 (2000), pp. 5660–5694.